Modern Ionospheric Ray Tracer for Earth Observation Satellite Missions

Carlos Molina, Elena Fernández-Niño, and Adriano Camps

***Abstract*—Electromagnetic waves propagation through the ionosphere is subject to several effects including refraction, absorption, signal delay, or Faraday rotation. A ray tracer propagator that simulates these effects is an important tool for all satellite missions relying on transionospheric communications and Earth observation. This study presents an update to the 1975 Jones and Stephenson IONORT's code by implementing the use of up-to-date ionospheric, atmospheric, and geomagnetic models (International Reference Ionosphere or NeQuick, NRLMSISE-00, and International Geomagnetic Reference Field), and a new 3-D model for equatorial plasma bubbles. The developed code is part of the Ionosphere Modular Software Package in the context of the European Space Agency project SIMIONO. High-frequency radar sounders, synthetic aperture radars, and GNSS reflectometry missions constitute the main application of this software. The ray tracer has been validated with respect to the original software and by comparing real versus simulated vertical ionograms in different locations and dates.**

***Index Terms*—Electromagnetic propagation, ionosphere, ray tracing, satellite communications.**

NOMENCLATURE

B_0	Earth's magnetic field (T).
c	Speed of the electromagnetic (EM) waves in free space (ms^{-1}).
e	Electron charge (C).
f	EM wave frequency (Hz).
f_c	Electron gyrofrequency or cyclotron frequency in the ionosphere, $\frac{\lvert e\rvert B_0}{2\pi m}$ (Hz).
f_p	Plasma frequency, $f_p = \sqrt{\frac{Ne^2}{4\pi^2\epsilon_0 m}}$ (Hz).
$\mathcal{H}$	Hamiltonian.
k_r, k_θ, k_φ	Wave vector $\overrightarrow{k}$ spherical coordinates (m^{-1}).
m	Mass of the electron (kg).
N	Ionospheric electron density (m^{-3}).
n	Complex phase refractive index.
r, θ, φ	Spherical polar coordinates (m, rad, rad).
t	Time (s).
ϵ_0	Electric permittivity of free space (Fm^{-1}).
θ	Colatitude in spherical polar coordinates (Angle wrt. North z-axis) (rad).
λ	Electromagnetic wavelength (m).
ν	Electron collision frequency (Hz).
P'	Group path $P' = ct$ (m).
φ	Longitude in spherical polar coordinates (East direction angle wrt. X-axis in the XY-plane) (rad).
Ψ	Angle between $\widehat{k}$ vector and $-\overrightarrow{B_0}$ (rad).
ω	$2\pi f$, angular wave frequency ($\mathrm{rad\,s}^{-1}$).

Manuscript received 3 November 2023; revised 5 March 2024 and 30 April 2024; accepted 18 June 2024. Date of publication 2 July 2024; date of current version 5 August 2024. This work was supported in part by project GENESIS: GNSS Environmental and Societal Missions–Subproject UPC under Grant PID2021-126436OB-C21 sponsored by MCIN/AEI/10.13039/501100011033/ and in part by EU ERDF "A way to do Europe." *(Corresponding author: Carlos Molina.)*

Carlos Molina is with the CommSensLab—UPC, Universitat Politécnica de Catalunya—BarcelonaTech, 08034 Barcelona, Spain, and also with the Institute of Space Studies of Catalonia (IEEC)—CTE-UPC, 08034 Barcelona, Spain (e-mail: carlos.molina@upc.edu).

Elena Fernández-Niño is with the CommSensLab—UPC, Universitat Politécnica de Catalunya—BarcelonaTech, 08034 Barcelona, Spain.

Adriano Camps is with the CommSensLab—UPC, Universitat Politécnica de Catalunya—BarcelonaTech, 08034 Barcelona, Spain, also with the Institute of Space Studies of Catalonia (IEEC)—CTE-UPC, 08034 Barcelona, Spain, and also with the UAE University, Abu Dhabi 15551, UAE.

Digital Object Identifier 10.1109/JSTARS.2024.3421509

I. INTRODUCTION

NOWADAYS, EM signals are transmitted and received all around the world for many purposes. Even before the appearance of satellites in the late 1950s, long-range Earth-to-Earth radio communications made use of the ionosphere, using the "reflection" observed in the "shortwave" radio spectrum, which approximately corresponds to the modern definition of high frequency (HF). These so-called skywaves were able to bounce back in the ionosphere allowing for very long-distance communications, even between different continents.

For both, Earth-to-Earth skywave communications, and Earth-to-satellite communications, it is very important to study the propagation of the EM through the ionosphere, as it may have a large impact on them. The main effects produced in EM waves crossing the ionosphere are as follows:

1) refraction, or bending of the direction of propagation;
2) absorption;
3) signal delay and phase advance;
4) dispersion, due to the dependence on the delay with the frequency within the signal's bandwidth;
5) Faraday rotation, due to the different accumulated phases of the ordinary and extraordinary rays;
6) intensity and phase scintillation, which are the rapid fluctuations due to the focusing of the wavefront due to the small-scale electron density irregularities

These effects highly depend on the characteristics of the transmitted wave (frequency and polarization), the geometry of the communications (elevation and azimuth angles), and the local ionospheric and magnetic field conditions, which depend on the geographical coordinates, local time (LT), date, and solar activity. Knowing these effects in detail is crucial to all space

sciences using EM waves through the ionosphere, in particular the ones operating at low frequencies. In addition to HF, very-high-frequency (VHF), and ultrahigh-frequency (UHF) Earth-to-space communications or vice versa, three remote sensing (RS) techniques are particularly affected by the effects of the ionosphere: L- and P-bands synthetic aperture radars (SARs) [1], global navigation satellite system (GNSS) or LEO-PNT [2] systems, and radar sounders [3].

SAR missions such as ALOS-PALSAR [4], ROSE-L [5], NISAR [6], SAOCOM [7], or BIOMASS [8], [9], all operate at L-band, except BIOMASS, which uses P-band. As SAR techniques use accurate phase measurements to create the synthetic aperture, small phase fluctuations due to the ionosphere can highly affect their performance producing blurred images.

GNSS also uses the accurate phase and delay measurements from the signals received from several GNSS satellites to derive the position of the receiver precisely. In regions of the Earth with high ionospheric variability geopositioning accuracy and reliability are degraded. GNSS can also be used as signals of opportunity to perform GNSS-radio occultation (GNSS-RO) or GNSS-reflectometry (GNSS-R). Therefore, GNSS-R and GNSS-RO techniques are also affected by the ionosphere.

Radar sounders can use MF, HF, and VHF radio waves to probe the subsurface of celestial bodies. They have been used on Mars to map the distribution of water ice and study the structure of the planet's crust. The MARSIS instrument, operating between 1.3 and 5.5 MHz, onboard the European Mars Express mission [10], and the SHARAD instrument at 20 MHz on NASA's Mars Reconnaissance Orbiter [11], are examples of this technique on Mars. However, its use on the Earth is more limited because of the higher electron density of the Earth's ionosphere. Some studies are examining the possibility of using up to 45-MHz signals to allow subsurface penetration [12]. The use of ray tracing tools at these frequencies is essential to simulate the ionospheric impact and asses the instrument's performance.

It is important to have a ray tracing tool for radio signals crossing the ionosphere to study all the effects listed previously and devise techniques to eventually mitigate them. Ionospheric scintillation is simulated using Rino's multiple phase screen model [13] using as inputs the outputs of the WBMOD [14]. Although, the ionospheric scintillation module is not the object of this article.

The development of this ray tracer was conducted in the frame of the European Space Agency (ESA) SIMIONO project. The project was coordinated by ONERA (France), who also developed SAR algorithms to compensate for ionospheric scintillation effects, RDA (Switzerland), who did the final coding and testing, and CommSensLab-UPC (Spain), who was in charge of the development of the scintillation module and the ray-tracer tool in MATLAB. These modules are part of the Ionosphere Modular Software Package [15] tool developed for ESA.

After a review of the bibliography and possible existing tools to simulate ray tracing through the ionosphere, the most interesting one was a FORTRAN implementation of a ray tracer from the 1970s. The code was available along with extensive documentation on the implementation details, including all the core equations and algorithms. The document "A Versatile Three-Dimensional Ray Tracing Computer Program for Radio Waves in the Ionosphere" by R. M. Jones and J. J. Stephenson [16] was published by the Office of Telecommunications of the U.S. Department of Commerce in October 1975. The report describes an accurate and versatile FORTRAN computer program for ray tracing EM rays through an anisotropic medium whose index of refraction can vary continuously. It originally aimed to simulate ionospheric ray tracing, but it could also be modified to simulate other scenarios. During the last 50 years, this program has been the most important and accurate existing ionospheric ray tracer, with no major updates or modifications to authors' knowledge.

Recently, a software package used the FORTRAN implementation as a subroutine inside a MATLAB GUI, which simplifies the input of variables and provides a visual representation of the results. This program was distributed under the name of IONORT [17], and it has had several versions in recent years [18], [19]. The drawback of this approach is that the core code is still written in FORTRAN, allowing limited modifications of the models used. In addition, the mix of FORTRAN and MATLAB languages forces the use of text files as a way to input/output the variables and results, which slows down the computation and adds complexity to the codes.

In [20] and [21], a wave propagation algorithm named IONOLAB-RAY is presented. It can trace rays in anisotropic, inhomogeneous, and time-varying ionosphere. The refractive index is computed using the Appleton–Hartree formula, after obtaining the physical parameters from models of the ionosphere such as the IRI-Plas-G [22], magnetic field from International Geomagnetic Reference Field (IGRF) [23], and atmospheric parameters from NRLMSISE-00 [24].

This article presents the update of the old FORTRAN code to a more up-to-date programming language such as MATLAB, easing its maintenance and updates, allowing the implementation of new features and more recent atmospheric, ionospheric, and geomagnetic models, such as International Reference Ionosphere (IRI) [25], NeQuick [26], IGRF, or NRLM-SISE.

MATLAB provides a rapid and simple, yet versatile and powerful, programming language. Later on, this MATLAB implementation was translated into C++ language by RDA to increase its performance and usability of the software by European Space Agency (ESA) in other simulation tools.

The rest of this article is organized as follows. Section II addresses the software description in comparison to its previous version and the new features included in the software presented, Section III presents several results obtained using the ray traced described, and finally, Section IV concludes this article.

II. Software Description

In this section, a complete description of the code is presented. Section II-A explains the part of the code that is inherited from the original FORTRAN routines. Section II-B describes the updated and the new models implemented in the code. Finally, Section II-C makes some useful remarks on the internal architecture of the software, and its inputs and outputs.

A. Brief Description of the Original Program

As stated in [16], several versions of this software were used for about 9 years before its publication in 1975, each of them

having continuous updates and improvements. The code calculates the refractive index by either the Appleton–Hartree [27] or the Sen–Wyller [28] formulas. It also has several ionospheric models for the electron density, the Earth's magnetic field, the electron collision frequency, and other perturbations (irregularities) of the electron density. For the mathematical description of this ray tracing software, the symbols used in this article are described in Nomenclature.

The way to compute the EM ray trace is by integrating the Hamilton equations in four dimensions, three spatial and one temporal, in which the spatial coordinates are given in spherical coordinates (r, θ, φ), and the temporal variable is t. In each step of the integration, the derivatives of each one of the four coordinates are expressed as derivatives of the Hamiltonian $(\mathcal{H})$. In addition, the three components of the wave vector $(k_r, k_\theta, k_\varphi)$ are computed as

$$\frac{dr}{dP'} = -\frac{1}{c}\frac{\partial \mathcal{H}/\partial k_r}{\partial \mathcal{H}/\partial \omega} \tag{1}$$

$$\frac{d\theta}{dP'} = -\frac{1}{rc}\frac{\partial \mathcal{H}/\partial k_\theta}{\partial \mathcal{H}/\partial \omega} \tag{2}$$

$$\frac{d\varphi}{dP'} = -\frac{1}{rc\sin\theta}\frac{\partial \mathcal{H}/\partial k_\varphi}{\partial \mathcal{H}/\partial \omega} \tag{3}$$

$$\frac{dt}{dP'} = -\frac{\partial \mathcal{H}}{\partial \omega} \tag{4}$$

$$\frac{dk_r}{dP'} = \frac{1}{c}\frac{\partial \mathcal{H}/\partial r}{\partial \mathcal{H}/\partial \omega} + k_\theta\frac{d\theta}{dP'} + k_\varphi\sin\theta\frac{d\varphi}{dP'} \tag{5}$$

$$\frac{dk_\theta}{dP'} = \frac{1}{r}\left(\frac{\partial \mathcal{H}/\partial \theta}{\partial \mathcal{H}/\partial \omega} - k_\theta\frac{dr}{dP'} + k_\varphi r\cos\theta\frac{d\varphi}{dP'}\right) \tag{6}$$

$$\frac{dk_\varphi}{dP'} = \frac{1}{r\sin\theta}\left(\frac{\partial \mathcal{H}/\partial \varphi}{\partial \mathcal{H}/\partial \omega} - k_\varphi\sin\theta\frac{dr}{dP'} - k_\varphi r\cos\theta\frac{d\theta}{dP'}\right). \tag{7}$$

The aforementioned derivatives are evaluated with respect to an independent variable that, in this case, has been chosen as the group path, P', because it is independent of the choice of the Hamiltonian used. This is also interesting because, this way, the integration steps will automatically reduce near reflections or high curvature points in the trajectory, where the calculations are more critical.

The version of the software used was the one implementing the Appleton–Hartree formula [27], which is the one that computes the refractive index as a function of the local plasma parameters. There are different versions of this formula, depending on whether the magnetic field and electron collisions are considered or not. The most complete one is with collisions and with magnetic field

$$n^2 = 1 - \frac{2X(1-iZ-X)}{2(1-iZ)(1-iZ-X) - Y_T^2 \pm \sqrt{Y_T^4 + 4Y_L^2(1-iZ-X)^2}} \tag{8}$$

where X, Y, and Z are three important frequency ratios

$$X = \frac{f_p^2}{f^2} \tag{9}$$

$$Y = \frac{f_c}{f} \tag{10}$$

$$Z = \frac{\nu}{2\pi f} \tag{11}$$

$$Y_T = Y\sin\Psi \tag{12}$$

$$Y_L = Y\cos\Psi \tag{13}$$

where all the variables are defined in Nomenclature.

The ray tracing steps are integrated using the numerical Runge–Kutta [29] method, with the possibility of using alternatively the Adams–Moulton method [30], [31], with an error prediction/correction algorithm. After each step, in the new position, the phase refractive index and its gradients are computed. In the original code, different subroutines implemented each model.

1) ELECTX: It computes the electron density at each position and its 3-D gradients. Using the plasma density, the plasma frequency is computed, and therefore, the X in (9). The original software required the user to input a `.txt` file with a gridded electron density model in discrete (latitude, longitude, and altitude) points.
2) ELECT1: This subroutine lets the user input a custom ionospheric electron density model or profile. As this is a perturbation to the electron density, it is also changing the effective plasma density and X. In the original software, any model was intrinsically defined, letting the user implement it.
3) MAGY: Computes the Earth's magnetic field, which translates into the cyclotron frequency f_c, and therefore, the magnitude Y in (10). In the original code, it was simply modeled as a magnetic dipole in the direction of the geomagnetic field by entering the coordinates of the North magnetic pole.
4) COLFRZ: Computes the electron collision frequency (ν) at the specified height, which sets the value of Z in (11). The method implemented was the double exponential equation described in the Section II-B4.

B. New Models Implemented

The general structure of the code and the algorithms used to solve the ray tracing equations are kept in the new updated code. The main updates have been implemented in the models that the simulator uses to compute the three most important parameters in the Appleton–Hartree formula [see (8)]: X, Y, and Z. Related to the X parameter, the electron density will be computed from the IRI-2016 model, and a model for equatorial plasma bubbles (EPBs) will be included [32]. The Y component will use the results from the IGRF geomagnetic model, and for the Z parameter, the electron collision frequency will be computed from four new models. All these updates are explained in detail in the following subsections.

TABLE I
SPACE WEATHER VARIABLES

K	Nonlinear index measuring geomagnetic fluctuations (0 to 9)
K_p	Planetary K index (weighted average global from K-indices)
a	3-hourly range linearized K index
A	Average of eight a-indices within a day
A_p	Planetary A index
F10.7	Hourly average of solar radio strength at 10.7 cm wavelength

1) Electron Density, the International Reference Ionosphere: The ionospheric electron density, N, is defined by the number of electrons per unit volume in the ionospheric plasma, usually given in m^{-3}. The largest oscillation in the value of the electron density follows a daily pattern, with larger densities during daylight, and smaller ones during the night. On top of that, it follows a seasonal variation, and it is also affected by the 11-year solar activity cycle, with higher values at higher solar activity periods.

The IRI [25] is an international project sponsored by the Committee on Space Research, and the International Union of Radio Science (URSI), which develop and maintain an empirical standard model of the ionosphere based on several available data sources. It provides monthly averages of electron density, electron temperature, ion temperature, and ion composition at altitudes that range from 60 to 2000 km.

The model is updated yearly using several data sources that include the worldwide network of ionosondes, incoherent scatter radars such as Jicamarca, Millstone Hill or Malvern, the ISIS and Alouette topside sounders, and other in situ satellites and rockets. The model is provided in FORTRAN subroutines, model coefficients (CCIR, URSI, and IGRF), and indices files (K_p, A_p, and solar flux F10.7, defined in Table I). The IRI model has had several versions: IRI-2001, IRI-2007, IRI-2012, IRI-2016 (last update in October 2021), and the most recent IRI-2020, released in 2020. The one implemented by default on this project was the IRI-2016 because it was the most recent implementation when the project started.

The outputs of the model are as follows:

1) electron density N (m^{-3});
2) electron temperature T_e (K);
3) neutral temperature T_n (K);
4) ion temperatures T_i (K);
5) ion composition $(O^+, H^+, He^+, O_2^+, NO^+, N^+)$ (%);
6) total electron content (TEC) (TECU);
7) layer peaks heights (F2, F1, E, D) (km);
8) layer peaks densities (F2, F1, E, D) (m^{-3}).

For the ray tracer simulator, only the electron density and temperature are used. The user has the option to provide a file containing an externally created ionospheric grid profile. If this file is not found, the program calls the IRI-2016 model [33], [34], and creates an IONO_PROFILE, consisting of a 3-D matrix of electron densities and temperatures, sampled at equally spaced grid points in latitude, longitude, and altitude. The structure also contains some additional information such as the coordinated universal time (UTC) time of the ionospheric profile, and the vectors indicating the grid vertices. Typically, grids are retrieved globally with an angular resolution of 5° and a vertical resolution of 5 km, but it can be defined by the user.

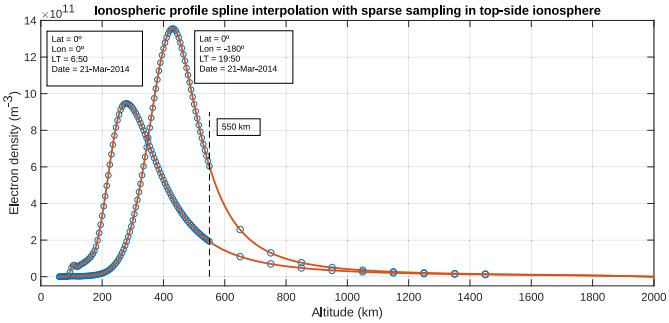

Fig. 1. Ionospheric profiles from the IRI-2016 model used in the simulator. Blue dots are the grid point samples, and the red line is the spline interpolator curve.

The simulator computes the electron density and the spatial gradients at every point in the integrated path by using a spline interpolator between grid points. To reduce data storage and computations, the vertical resolution has been computed with a sparser sampling at altitudes above 550 km, where the ionosphere has already crossed the peak density and starts to smoothly tend to zero. Two different ionospheric profiles are represented in Fig. 1, for the same time on 21 March 2014, but different longitudes, and therefore, different LT.

Using the electron density computed from the IRI model, the value of $X = f_p^2/f^2$ is computed, where the plasma frequency, in megahertz, is obtained as

$$f_p^2 = \left(\frac{\omega_p}{2\pi}\right)^2 = \frac{10^{-12}}{4\pi^2}\frac{e^2\,N}{m\epsilon_0} = \frac{N}{1.244\times 10^{10}}. \tag{14}$$

2) Electron Density Perturbations, Bubbles, and Depletions: The ionosphere is far from being a stable layer, and it suffers from several perturbations in its plasma density and its dynamics. Apart from the already mentioned relatively smooth daily, seasonal, and with the solar cycle variations, the ionosphere exhibits local perturbations in time and space, which are much more difficult to model or predict. In particular, many studies in the last decades have shown the occurrence of EPBs, which usually appear after sunset, move Eastwards along the constant magnetic field lines for a certain time, and then, disappear.

In this part of the software, a 3-D model has been implemented based on the climatological data on its size, shape, duration, position, and horizontal speed retrieved from the works by Blanch et al. [32] in a precursor ESA project. The data are obtained from lookup-tables (LUT) indicating the probability density distribution for the variables mentioned before. With these values, a set of bubbles is generated with random positions, sizes, shapes, and durations meeting the probability distributions for this time and location. The mathematical details of the model used are described in the Appendix.

Using the proposed model, Fig. 2 shows the results of a realization of the bubbles at 21 March 2014 06:50 UTC. The colors

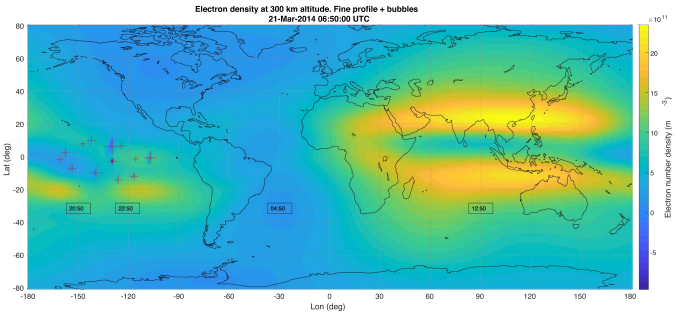

Fig. 2. Perturbed electron density at 300-km altitude after applying the bubbles model for the March equinox 2014, a peak in the solar activity. In the Pacific equatorial region, 12 EPBs appear marked with red crosses proportional to their diameters. Note that the LT of the region where the bubbles appear is between 20 and 22 h.

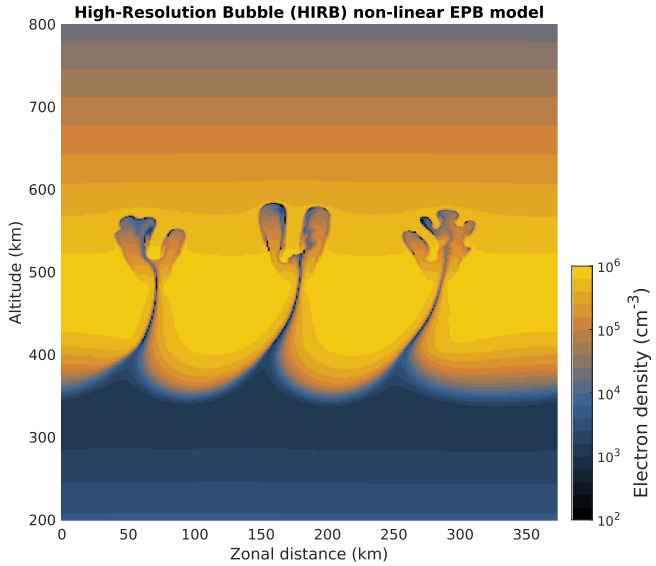

Fig. 3. Representation of the Yokoyama 3-D high-resolution bubble (HIRB) nonlinear EPB model for $T = 3000$ s. Using available dataset [41] of [40, Fig. 4].

represent the electron density at an altitude of 300 km, which represents the addition of the background IONO_PROFILE for this time, and the ΔN modeling the bubbles. It can be observed that 12 bubbles appear in the region in which the LT corresponds to the period in which it is more probable to find bubbles, from 20 to 22 h.

The model proposed in this study for EPBs is rather simple, but it is already an improvement with respect to the 2-D statistical model from [32]. Bubbles are known to have a more complex structure, appearing as curved shells traveling along the magnetic equator [35], [36], [37]. More recent studies [38], [39], [40] have worked on the numerical simulation of equatorial plasma depletions, yielding much more complicated shapes derived from a nonlinear turbulent ascension of the bubble. An illustration of these results using the simulation data from [41] is shown in Fig. 3. Using these results to improve the ray tracer will be the object of future works.

3) Magnetic Field, International Geomagnetic Reference Field (IGRF): The Earth's magnetic field is produced by the rotation of the internal layers of magma. This field can be roughly approximated by a dipole, as it was the approach in the original FORTRAN code. However, the Earth's magnetic field has a much more complex description. Its shape and intensity also vary with time, which makes it necessary to continuously update the model.

The IGRF is the most internationally accepted model to describe the Earth's magnetic field. IGRF was produced and is maintained by the International Association of Geomagnetism and Aeronomy since 1965 [42]. It describes the Earth's magnetic field in epochs from 1900 to 2020, with a secular variation prediction up to 2025. Last versions are the 12th [43], and the 13th [23]. The IGRF-13 updates the model marking epochs from 1945 to 2015 definitive (named DGRF). From IGRF-12, the coefficients are defined up to tenth degree with a 1-nT precision for epochs 1995 and before, and for epochs from 2000 onwards, they are defined up to 13th degree with a precision of 0.1 or 0.01 nT, depending on whether it is a definitive or nondefinitive version. The same precisions are maintained in the IGRF-13. The precision of the secular version for the last epoch in each version (i.e., 2020–2025 in IGRF-13) is specified up to eight degree.

There is another global magnetic model internationally accepted, which is the World Magnetic Model (WMM) [44], [45]. The main difference between IGRF and WMM is that the WMM is a predictive-only model, only valid for the 5 years in the current epoch (2020.0 to 2025.0 at present). In terms of precision, they are both very similar with relative differences between them of less than 0.1 nT for magnetic intensities in the order of 10^5 nT, and inclination/declination values of less than 0.1°, as compared by Oehler et al. [46].

4) Electron Collision Frequency, Attenuation: The attenuation or absorption suffered by the EM wave crossing the ionosphere is mainly due to the imaginary part of the complex phase refractive index, n. In the code, the absorption computation has not been changed from its original definition, as described in [16]

$$\frac{dA}{dP'} = \frac{10}{\ln 10} \cdot \frac{\text{imag}\left(\frac{\omega^2}{c^2} n^2\right)}{k_r^2 + k_\theta^2 + k_\varphi^2} \cdot \frac{k_r \frac{\partial \mathcal{H}}{\partial k_r} + k_\theta \frac{\partial \mathcal{H}}{\partial k_\theta} + k_\varphi \frac{\partial \mathcal{H}}{\partial k_\varphi}}{c \frac{\partial \mathcal{H}}{\partial \omega}}. \tag{15}$$

The main contributor to the imaginary part of the refractive index of the ionosphere comes from the electron collision frequency. The electron collision frequency is the rate at which electrons in the ionized plasma are colliding with neutral atoms or ions within the plasma. Given that, the total electron collision frequency is given by the addition of the electron-neutral (ν_{en}), and electron-ion (ν_{ei}) collision frequencies

$$\nu_e = \nu_{\text{en}} + \nu_{\text{ei}}. \tag{16}$$

This value, in general, is difficult to estimate in the ionosphere because the collision frequency involves the cross-sectional parameter between the colliding particles, which is a function of the particles' velocity. The particle velocity is related to the gas temperature and density, but also to the interaction potential between the particles, which is well-defined by the Coulomb potential in the case of charged particles as electrons with ions,

but it is not very well-defined for neutral particles, and it should be derived from experimental data.

In the old FORTRAN model, a simple double exponential model [16] was used to compute the electron collision frequency as a function of the altitude. In this case, there was no distinction between neutral or ion collisions, but according to its shape, it is likely to be modeling only the electron-neutral collisions. This double exponential method is given by

$$\nu = \nu_1 e^{-a_1(h-h_1)} + \nu_2 e^{-a_2(h-h_2)} \tag{17}$$

where

$$\nu_1 = 36500.0\,\text{Hz} \qquad \nu_2 = 30.0\,\text{Hz}$$
$$h_1 = 100.0\,\text{km} \qquad h_2 = 140.0\,\text{km}$$
$$a_1 = 0.1480\,\text{km}^{-1} \qquad a_2 = 0.0183\,\text{km}^{-1}.$$

The double exponential method is a very simple model of the electron collision frequency, and it does not take into account the changes in gas densities and temperatures due to the daily or seasonal evolution. To portray these factors in the collision frequency, the physical equations or models that use the gas densities and temperatures have to be implemented. A total of four additional approaches to compute the electron collision frequency have been implemented in the code, using models from past studies.

The simpler collision frequency to compute is the electron-ion collision frequency because the governing interaction between these particles is the Coulomb potential. To model this collision frequency, Nicolet's equation (1953) is used [47]

$$\nu_{\text{ei}} = \left(34 + 8.36\log_{10}\frac{T^{3/2}}{N^{1/2}}\right) NT^{3/2} \tag{18}$$

which will be valid in the upper ionosphere as the electron-ion collisions are dominant in the F-layer because of the electron density, and therefore, the total ion density is the largest one.

For the lower part of the ionosphere (D-layer), the electron-neutral collisions are the dominant term. To compute its value from the gas densities, two different methods have been implemented in the software. The first one is also coming from Nicolet's works [47]. The electron collision frequency ν_{12} between particles of type 1 and particles of type 2 is

$$\nu_{12} = \frac{16}{3}\frac{n_1 m_1 + n_2 m_2}{m_1 + m_2}\pi\sigma_{12}^2\sqrt{\frac{(m_1+m_2)K_B T}{2\pi m_1 m_2}} \tag{19}$$

where m_1 and m_2 are the particles masses, n_1 and n_2 are the number densities, T is the absolute temperature, K_B is the Boltzmann constant, and σ_{12} is the effective collision distance between the particles.

For electrons of mass m_e, neutral particles of mass m, and number density n, since $m \equiv m_1 \gg m_2 \equiv m_e$, (19) becomes

$$\nu_{\text{en}} = \frac{4}{3}n\pi\sigma^2\sqrt{\frac{8K_B T}{\pi m_e}}. \tag{20}$$

This means that the collision frequency can be estimated from the effective collision distance between electrons and neutrals, but this is not easy to estimate for low-velocity electrons in the ionosphere.

TABLE II
COLLISION FREQUENCY MODELS IMPLEMENTED IN THE RAY TRACER

W.col_freq	Collision frequency model implemented
1	Double exponential model
2	Nicolet electron-neutral
3	Nicolet electron-neutral + Nicolet electron-ion
4	Schunk–Nagy electron neutral
5	Schunk–Nagy electron-neutral + Nicolet electron-ion

The constant kinetic cross section, $Q = \pi\sigma^2$, could be an approximation to the value of the effective collision distance. For low-energy electrons, the correspondence between the theoretical values of Q and the experimental measurements decreases. [48] gave some results comparing the experimental and theoretical results when the electron's energy is between 0 and 1 eV, and in general, the experimental values are larger than the theoretical ones. For oxygen (O_2) at 0.7 eV, $Q = 12$ a.u.[1] in theory, but $Q = 19$ a.u. experimentally. At the same energy, for Nitrogen (N_2), $Q = 17$ a.u. in theory, but $Q = 30$ a.u. experimentally. This method has been implemented in the ray tracer code using a default value of $Q = 15$, but it can be modified by the user.

In addition, another method to compute the electron-neutral collision frequency has been implemented in the software. The Schunk–Nagy electron-neutral collision frequency [49], a result from *Banks* [50], was implemented too. This frequency is computed from the contribution of the different neutral species in the ionosphere, namely N_2, O_2, atomic oxygen, atomic hydrogen, and He as follows:

$$\nu_{\text{en}} = \nu_{eN_2} + \nu_{eO_2} + \nu_{eO} + \nu_{eHe} + \nu_{eH} \tag{21a}$$
$$\nu_{N_2} = 2.33\cdot 10^{-11}\, n(N_2)(1 - 1.21\cdot 10^{-4}T_e)T_e \tag{21b}$$
$$\nu_{O_2} = 1.82\cdot 10^{-10}\, n(O_2)(1 + 3.6\cdot 10^{-2}\sqrt{T_e})\sqrt{T_e} \tag{21c}$$
$$\nu_{O} = 8.9\cdot 10^{-11}\, n(O)(1 + 5.7\cdot 10^{-4}T_e)\sqrt{T_e} \tag{21d}$$
$$\nu_{H} = 4.5\cdot 10^{-9}\, n(H)(1 - 1.35\cdot 10^{-4}T_e)\sqrt{T_e} \tag{21e}$$
$$\nu_{He} = 4.6\cdot 10^{-10}\, n(He)\sqrt{T_e} \tag{21f}$$

where $n(\,)$ are the number densities (m^{-3}) of each of the gas species, and T_e is the electron temperature. Knowing the values of each number density, and the electron temperature at each altitude, the collision frequency can be derived.

The purpose of `col_freq.m` is to compute the collision frequency at a given position and time using the model selected by the user-defined parameter `W.col_freq` from Table II.

The required values of the electron density (N) and the temperature (T_e) are obtained from the IRI-2016 model, previously described. The atomic and molecular densities (n(gas)), and total neutral's densities (n) are obtained from the atmospheric model NRLMSISE-00 [24].

The NRLMSISE-00 is an empirical, global reference atmospheric model developed by the U.S. Naval Research Laboratory (NRL) using the mass spectrometer and incoherent scatter (MSIS) radar data, and it extends up to the exosphere. It takes

[1] Values of Q in atomic units (a.u.). 1 a.u. $= 2.8\cdot 10^{-17}\,\text{cm}^2$

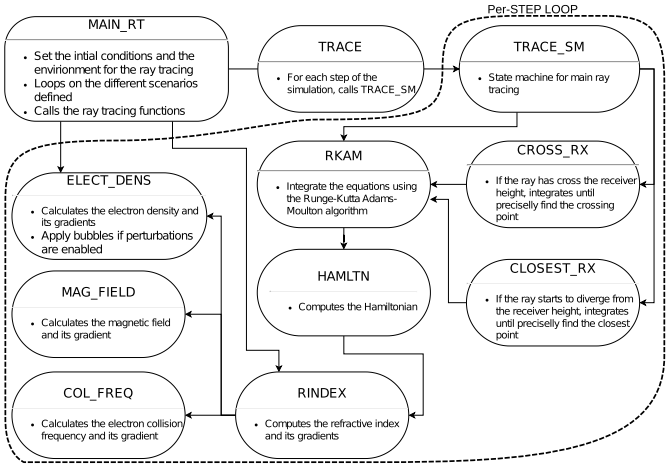

Fig. 4. Block diagram of the ionospheric ray tracing software and a short description of its functions. Arrows represent calls between functions.

as inputs the date and time (UTC), the geodetic altitude from 0 to 1000 km, the geodetic position (lat, lon), the 81-day average, and previous-day F10.7 solar flux, and the daily magnetic index (A_p). Its outputs include the number density of each atomic species, the total mass density, the exospheric temperature, and the temperature at each altitude. This model is implemented in the code using the MATLAB package: "NRLMSISE-00 Atmosphere Model" [51].

C. Software Architecture

Fig. 4 describes the program's internal blocks and its architecture, detailed in the following paragraphs.

The inputs are defined within a struct variable called W, which is set before running the software. This structure contains the fields and default values specified in Table III.

Some input parameters need a more detailed description. `W.frequency`, `W.azimuth`, and `W.elevation` can accept a vector of values to perform a sweep along the indicated values. The total number of simulations is the product of the lengths of each vector. Values within each vector are arbitrary and can be equispaced or not.

The hops are each portion of the path that the ray travels without "touching" the ground. From the transmitter until the first ground cross (or until the end of the ray tracing simulation if it escapes the Earth) belongs to the first hops. Then, every time the rays reflect on the ground surface, the hop number increments by two. For example, if a complete three-hop tracing has to be simulated, `W.max_hops` must be set to 5, as shown in Fig. 5. It can be observed that the internal variable `h` counting the hops, is 1, 3, and 5 in each hop, respectively. After the second reflection on the ground, this variable would rise above 5, and therefore, the simulation will stop. Finally, the `W.max_steps` sets the maximum number of steps to be computed within each hop. Starting a new hop, the step count is restarted. If the hop is too long, the step size is too short, or the ray escapes to space, the simulation will also stop.

TABLE III
INPUT PARAMETERS OF THE SIMULATOR

Field	Default value	Units	Description
W.date	[2014 03 21 6 50 00]		UTC date and time [yyyy mm dd HH MM SS]
W.time_step	0	s	Time step for temporal simulation
W.duration	0	s	Duration of temporal simulation (if null, no temporal simulation is performed)
W.ray_type	1		1: ordinary ray, -1: extraordinary ray
W.tx_height	800	km	Transmitter height above ground (>0 km)
W.tx_lon	2.1543	º	Transmitter longitude (-180º to 180º)
W.tx_lat	41.3905	º	Transmitter latitude (-90º to 90º)
W.frequency	50	MHz	Frequency sweep
W.azimuth	0	º	Azimuth sweep (0º to 180º)
W.elevation	-60	º	Elevation sweep (-90º to 90º)
W.rx_height	0	km	Receiver height above ground (>0 km)
W.max_hops	1		Maximum number of hops
W.max_steps	500		Maximum number of steps per hop
W.int_model	2		Numerical integration mode is Adams-Moulton without error checking (Not settable)
W.max_err	0.0001	km	Maximum allowable single step error
W.err_ratio	50		Ratio between maximum to minimum single step error
W.init_step	3	km	Initial integration step length
W.step_max	100	km	Maximum step length
W.step_min	0.001	km	Minimum step length
W.step_fact	0.5		Factor by which to increase or decrease step length
Electron density perturbations			
W.pert	FALSE		True if electron density perturbations are computed
W.bub_seeds	[1 1 1 1 1 1]		Integer seedsRandom number generator for bubbles parameters
W.fine_latlon_res	1	º	latlon fine resolution for perturbed IONO_PROFILE
W.fine_alt_res	5	km	height fine resolution for perturbed IONO_PROFILE
Geomagnetic field			
W.magmod	2		1 for dipole model, 2 for IGRF
W.gyrofreq_0	0.8	MHz	Gyrofrequency at the ground
Electron collisions			
W.collisions	TRUE		True to use collision frequency model
W.col_mode	2		1 for double exponential model, 2 for NRLMSISE-00
Space weather variables			
W.f107A	150	s.f.u.	81-day average of F10.7 flux (centered on doy)
W.f107	150	s.f.u.	Daily F10.7 flux for previous day
W.ap	4		Magnetic index
Output format			
W.verbose			True to activate verbose debugging prints

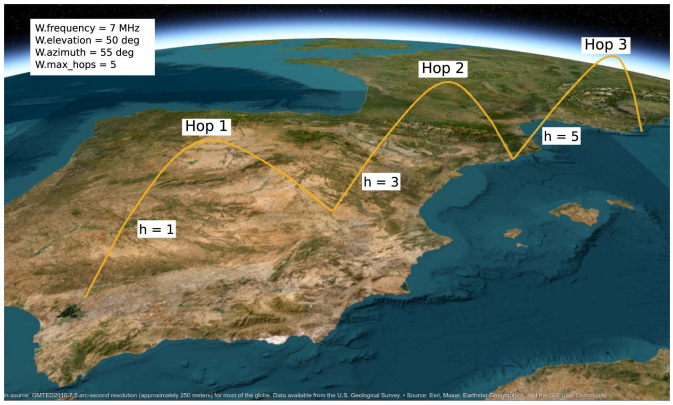

Fig. 5. Simulation of a ray traced from Seville (Spain) in the direction to Barcelona with an elevation of 50° to illustrate the concept of "hops." Each time a new hop is started, the internal variable `h` is increased by 2.

If the electron density perturbations are activated, `W.bub_seeds` are the random number generator seeds for the following bubble parameters: central latitude, central longitude, depth, duration, velocity, and temporal position of the maximum depth. Keeping the same seed for a parameter will fix this parameter for every call to the program. There is

also a fine resolution parameter for the IONO_PROFILE, which must be set in the order of the bubbles' dimensions to properly model them.

For the geomagnetic variables, the `W.gyrofreq_0` is only used for the dipole model, and the default value is inherited from the old implementation.

The space weather inputs detailed in the table are passed as inputs to the IRI and NRLMSISE models to override their computed values. If they are not provided, they are computed from the UTC date using the input files provided by each model [34], [51].

The main program is executed from the MATLAB function `main_rt.m`, and it is responsible for the creation of the environment in which the ray (or rays) will be traced, and the storage of the results. In the first stage, this function reads all the input variables and sets an environment in terms of date and time, ionospheric and atmospheric profiles, ray type (ordinary or extraordinary), electron collision model, or ionospheric perturbations if they are activated. Then, the program sets the initial condition of the ray or rays to be traced, adjusting the coordinates of the transmitter (latitude, longitude, and height), azimuth, elevation, and frequency.

Internal variables are initialized, and the script starts calling other functions to compute the propagation of each ray. This can only happen if, at the initial position, the plasma frequency is smaller than the wave frequency. If it is not possible, it is said that the transmitter is located in an evanescent region, and the transmission cannot start, yielding a warning message. If the transmission is possible, the program calls the ray tracing functions. The propagation is computed iteratively until a *stop condition* detailed later, is reached.

The ray tracer algorithm consists of a state machine in `TRACE_SM` that iteratively calls the integration and propagation functions while any of the stop conditions are satisfied. The stop condition ends the ray tracing and there are the following three cases.

1) Maximum number of steps reached in the current hop.
2) The ray has reached the closest distance to the desired receiver height, and it has started separating from it.
3) The ray has crossed the receiver height, and it is the last hop.

The state machine also checks if the ray has just crossed the Earth's surface to generate a reflection by changing the vertical component of the wave vector. In the case of a ground reflection, the code finds the ground-crossing point with a precision smaller than the integration step size.

For a normal propagation step, the state machine calls the functions to perform the integration of the ray coordinates by applying the Runge–Kutta algorithm (fourth-order Runge–Kutta, or RK4) [29] or the Adams–Moulton method with—or without—error prediction/correction algorithm [30].

When the simulation ends, the results are stored in a structure organized as shown in Fig. 6.

One instance of "path" per ray simulated is stored in the "ray" output. For each path, a list of variables are output. `Frequency`, `elevation`, and `azimuth` identify the ray simulated. The rest are vectors with the height of the number of steps performed in each ray, containing in-path parameters, such as the coordinates, the refractive index along the path (`n_2`), the accumulated `absorption`, the `group_path`, P', the `delay` (P'/c), and the electron density along the path (N). Using the electron density at each point, the user can then compute the slant TEC. This can be done by integrating N along the path using the geometric distance between the points of the path.

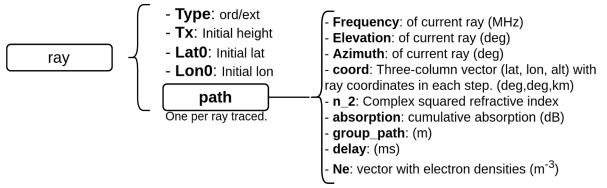

Fig. 6. Diagram of the "ray" struct, output of the ray tracer simulator.

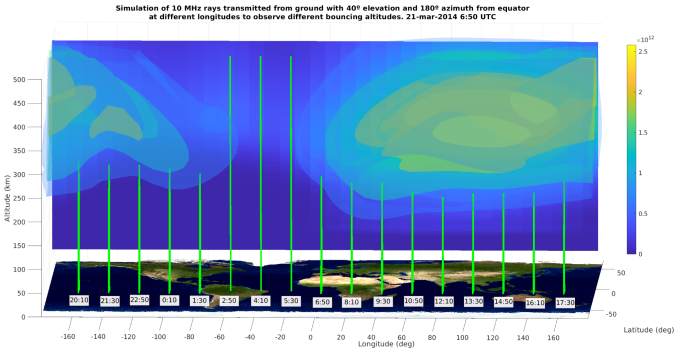

Fig. 7. Simulation of different zenithal rays transmitted at different longitudes in which the altitude reached depends on the local ionospheric profile. Bubbles in colors are electron density isosurfaces indicated in the color bar. Bottom labels indicate the LT. Altitudes not to scale.

The computation time per ray traced is usually around 10 s, depending on the step size and number of hops. The time required to compute the ionospheric profile grid at the beginning of the simulations is usually not longer than 30 s when the box size is restricted to ±10° around the transmitter coordinates in steps of 5°. These performance parameters are obtained using an Intel Core i7-4710HQ at 2.5 GHz, with 8 GB of RAM, running Ubuntu 22.04.4 LTS.

III. Results

To illustrate the fundamental phenomena occurring during the propagation of an EM wave through the ionosphere, and validate the implemented software, a suite of scenarios is simulated. In particular, the behavior of ordinary and extraordinary waves, the refraction, the absorption, and the performance of the EPBs model have been tested. Finally, a validation with respect to real-world measurements is presented by simulating vertical ionograms.

A. Verification of Common Phenomena

In Fig. 7, a scenario is presented where multiple zenithal rays are transmitted from the equator at distinct longitudes. These rays operate at 10 MHz, a frequency close to the usual plasma

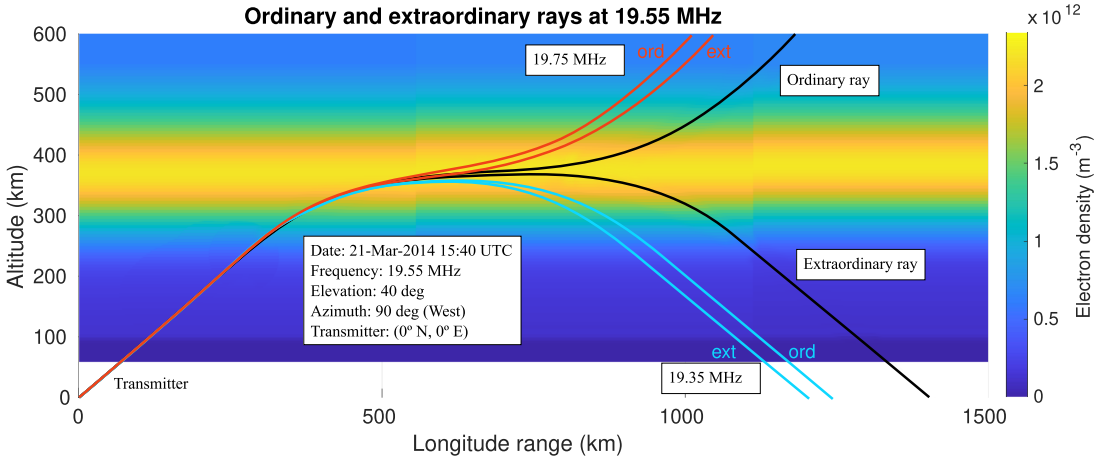

Fig. 8. Three oblique rays with frequencies around 19.55 MHz. Ordinary and extraordinary rays are plotted, showing that at the lower frequency (blue), none of them cross the ionosphere, at the highest frequency (red), both rays cross, and at the central frequency (black), the ordinary and extraordinary rays diverge.

frequency. Some can penetrate the ionosphere, while others are reflected back to Earth at varying altitudes. The simulations were conducted at equal UTC time for all rays, with the LT differing at various longitudes, as indicated in the bottom label. Vertical segments indicate up to which height the wave propagates until it reflects back to Earth. Three rays transmitted during the night at 2:50, 4:10, and 5:30 h LT can escape the ionosphere.

B. Ordinary and Extraordinary Rays

When an EM wave traverses the ionosphere, the anisotropy of the ionosphere induces a birefringence effect, resulting in two distinct propagation modes: the ordinary and the extraordinary rays. These two rays have different polarizations, and experience different refractive indices along their paths, leading to differences in the trajectory, delay, phase, absorption, and other parameters. The implemented ray tracer includes this effect and allows the selection of the ray type (extraordinary or ordinary) in the simulation.

At higher frequencies, this effect is small, causing just slight disparities in the propagation speed of each polarization, which results in the so-called Faraday rotation. However, at frequencies near the ionosphere cutoff frequency, these effects become more pronounced. In the presented example, a ray is transmitted from the ground with an elevation of 40°. At a specific frequency, both the ordinary and the extraordinary rays diverge from each other upon reaching the maximum ionization altitude. As depicted in Fig. 8, the ordinary ray at 19.55 MHz (in black) successfully penetrates the ionosphere and escapes the Earth, whereas the extraordinary ray reflects back to Earth. This phenomenon occurs within a narrow frequency band, contingent on geometric and environmental conditions. In this instance, 200 kHz above both rays transverse the ionosphere (in red), while 200 kHz below both rays undergo a total reflection (in light blue). It is noteworthy that the transmitter is located at the equator, where ionospheric density is near its maximum, explaining the relatively high frequency at which this effect manifests.

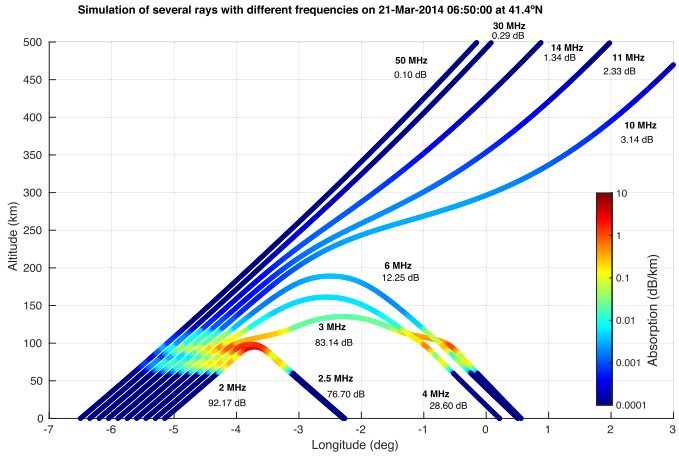

Fig. 9. Two-dimensional view of the ray paths for each frequency, showing the absorption in colors (log scale).

C. Absorption and Collision Frequency Models

The absorption of the EM signals depends on the frequency, and on the electron collision frequencies, which are very related to the densities of electrons, ions, and neutrals. In this section, several tests are shown to check the proper behavior of the simulator in this aspect.

First, an inclined ray transmitted from the Earth with a variable frequency is simulated to show the different bending and absorptions suffered. The frequencies vary from 2 to 50 MHz, and the inclination for all of them is 40°. The date of the simulation is 21 March 2014 at 6:50 UTC in the region of Spain (Latitude: 41.4° N, Longitude: −6° to 2°), so the LT is also around 6:50 h. The azimuth is set to 90°, so they travel in planes with the same latitude toward the East. Fig. 9 is a 2-D plot for the ray paths indicating in colors the absorption rate in dB/km. Labels indicate the frequency and the total absorption for each ray. The absorption versus the frequency is plotted in Fig. 10. In a log–log

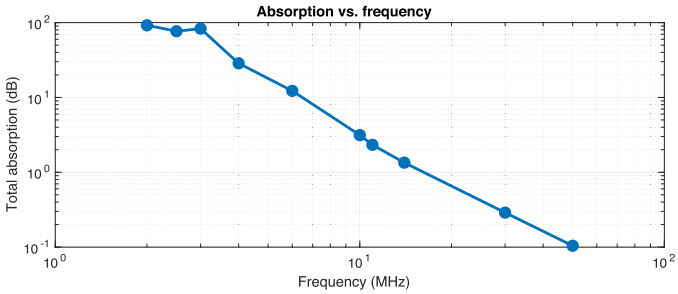

Fig. 10. Total absorption versus frequency in a log–log plot.

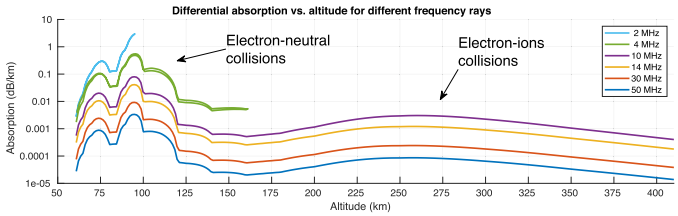

Fig. 11. Frequency sweep showing the absorption as a function of the altitude.

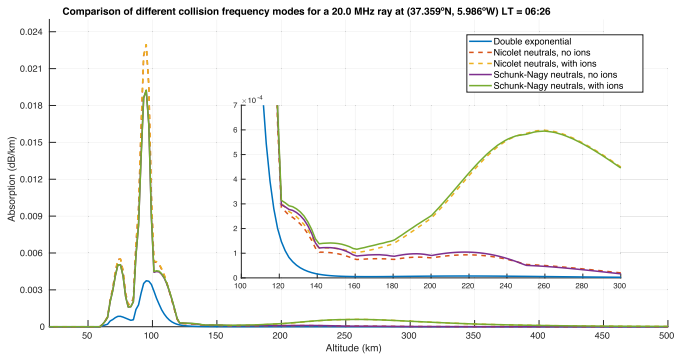

Fig. 12. Absorption versus altitude for each collision frequency model for a 20-MHz vertical ray over Spain (37.36° N, 5.99° W), on 21 March 2014 6:50 UTC, approximately corresponding to 6:26 LT.

representation, the absorption is approximately a linear function of the frequency, with slope ~ -2 above ~ 3 MHz.

To understand where this absorption is occurring, a plot versus the altitude is shown in Fig. 11, in which only a subset of the previous rays is shown. Rays with frequencies of 2 and 4 MHz do not cross the ionosphere, and bounce back to the Earth. In this figure, the regions in which the absorption is happening can be distinguished. The lower part, around 100 km is mainly due to the electron-neutral collisions, and in the top-side ionosphere, around 250 km, this absorption is due to the electron-ion collisions. Note that for this simulation, the collision frequency model 5 has been used, applying Schunk–Nagy's equation (21a) for the neutrals, and taking into account the ions with Nicolet's equation (18).

In the continuation of this section, the objective is to compare the five distinct collision frequency models incorporated into the ray tracer. To achieve this, a vertical ray at 20 MHz is traced with each of the five different models. Fig. 12 illustrates the

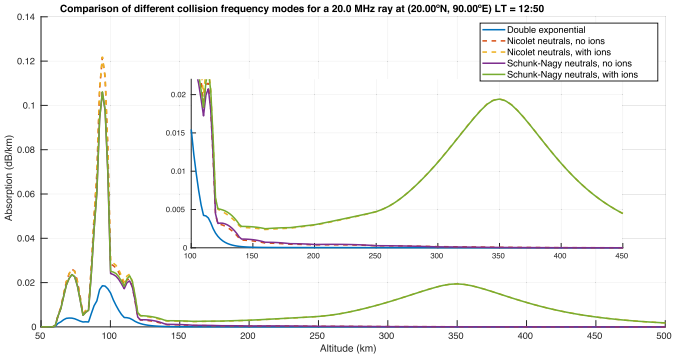

Fig. 13. Absorption versus altitude for each collision frequency model on March 21 2014 at daytime over Bangladesh (LT = 12:50 h).

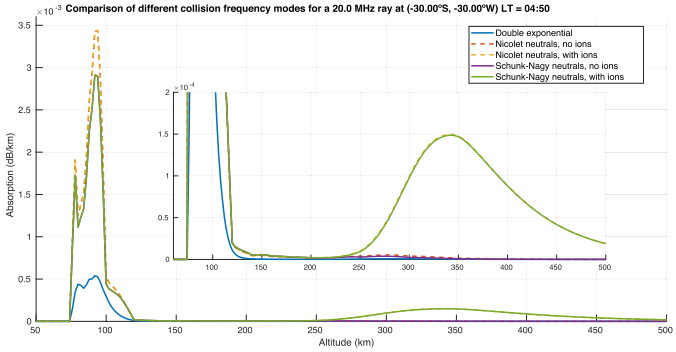

Fig. 14. Absorption versus altitude for each collision frequency model on March 21 2014 nighttime over Southern Atlantic (LT = 04:50).

absorption rate as a function of the altitude for the 20 MHz ray. The simulation is conducted at a specific point where the LT is 6:30, and the TEC is measured at 14.87 TECU.

As observed in previous results, it is clear that the largest absorption rate is located in the D and E layers, at altitudes around 70 and 100 km, respectively. The peak using the collision model 1 (double exponential method) underestimates the absorption with a much smaller magnitude than the other four, about 5 times smaller.

Comparing the rest of the collision frequency models (2–5), it can be seen that above an altitude of 150 km, models 2 and 4 decrease to zero because they do not take into account the collisions with ions, as models 3 and 5 do. As a final remark, using the Schunk–Nagy for the neutrals (solid lines) makes a slightly lower absorption value under 120 km. In particular in Fig. 12, Nicolet's neutrals (models 2 and 3) reach 0.193 dB/km, while the Schunk–Nagy model only gets to 0.163 dB/km. However, above 120 km, the behavior is the opposite.

To study the changes from day to night, two more simulations are presented for the same time at locations with different local times. Fig. 13 depicts the results for a daylight scenario in a region with a high-density ionosphere. The vertical ray is traced at a location in Bangladesh (41° N, 77.5° E) with an electron density near the maximum, specifically TEC = 38.18 TECU. In contrast, Fig. 14 shows the results for nighttime conditions at a point in the Southern Atlantic (30° S, 30° W), where the TEC is substantially lower: 4.66 TECU.

TABLE IV
TOTAL ABSORPTION FOR EACH COLLISION FREQUENCY MODEL FOR A 20 MHZ VERTICAL RAY DURING THE NIGHT (LT: 04:50) AND DAY (LT: 12:50)

W.col_mode	Night (dB)	Day (dB)
1	0.013	0.422
2	0.059	0.934
3	0.080	3.830
4	0.051	0.837
5	0.072	3.733

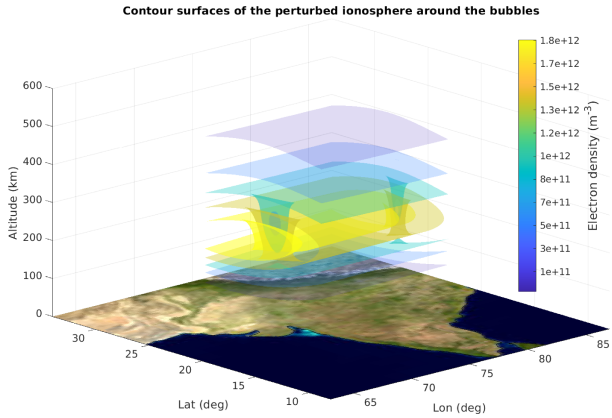

Fig. 15. Bubbles' 3-D electron density contours.

The absorption during the day reaches a peak of around 0.45 dB/km in the E-layer, which is about 25 times larger than during the night. The fusion of the D and E layers during the night is also visible, which are more separated during the day. The last difference observed from night to day is that the F layer absorption is displaced upwards, creating a larger space between the E layer with negligible absorption. The numerical results for the total absorption computed in these simulations are shown in Table IV.

D. Simulation of Bubbles and Depletions

In this section, perturbations have been added to the ionospheric profile in the shape of "bubbles" to try to simulate the effects of EPB in the propagation of EM waves. According to the EPBs model described in the previous section, when including perturbations in the simulation, during high solar activity periods, several bubbles (up to 10, at most) can appear just after sunset. Their quantity, position, depth, and size are given by their statistical values contained in a suite of LUTs [32].

In the following example, a scenario on March 14 2014 at 14:45 h UTC is simulated with two bubbles, as shown in Figs. 15 and 16. The resulting disturbed ionospheric profile has been computed with a resolution of 0.05° in horizontal and 5 km in vertical, getting to the one shown in Fig. 15 using isodensity contour surfaces. It can be seen that the centers of the bubbles are located near the maximum of the undisturbed profile. The vertical integration of this profile yields the vertical total electron content (VTEC) shown in Fig. 16.

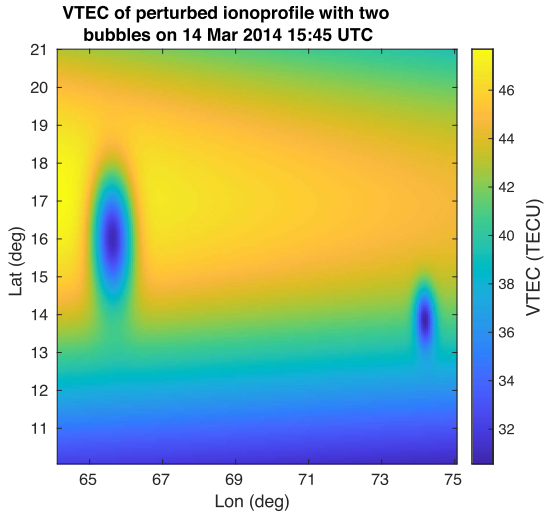

Fig. 16. Vertical total electron content (VTEC).

Then, several rays are traced through the bubble to study the perturbations suffered by them. The selected bubble for this experiment is on the left side of Fig. 16, located at (16.07° N, 65.65° E) with depth −15.9 TECU. Several vertical rays are traced by sweeping the latitude of the transmitter position, located at 650 km, and transmitting a 12-MHz signal to the ground. Results are shown in Fig. 17.

The plot shows the path of the rays through the background ionospheric profile. Each ray is additionally drawn indicating the real part of the squared refraction index (n^2). It can be seen that the ionospheric depletion reduces the density of the ionosphere so that the ray travels more similarly as if there was no ionosphere in this region.

E. Validation of the Ray Tracer Results Using Real Ionograms Data

A comparative analysis between actual ionogram data and the corresponding simulations generated by the ray tracer software has also been performed. Ionograms are the historical method to sense the ionosphere, being always one of the main ways to monitor and model ionospheric features, and changes. This technique involves transmitting near-vertical incidence skywaves from a ground antenna and receiving the subsequent echoes from reflections in the ionosphere. By measuring the signal delay at each frequency, the ionospheric profile can be estimated—at least, its bottom side. The frequency at which EM waves can escape to outer space, i.e., the maximum usable frequency (MUF), gives information on the ionospheric peak electron density and its altitude.

The Ionogram Data Base is an open-access database of ionograms that is maintained by the Global Ionosphere Radio Observatory [52], deployed in 2001 at the University of Massachusetts Lowell (UML). They provide real-time and historical ionosonde data gathered by a global network of 64 Digisonde locations in 27 countries [53], which can be used in this study to compare simulated ionograms with ground-truth data. Monte-Carlo

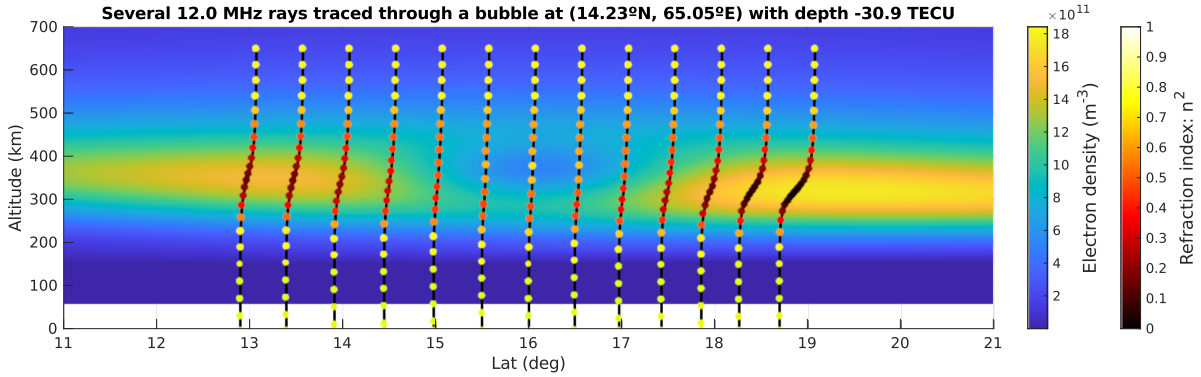

Fig. 17. Several 12-MHz-rays traced vertically around a bubble on 14 March 2014.

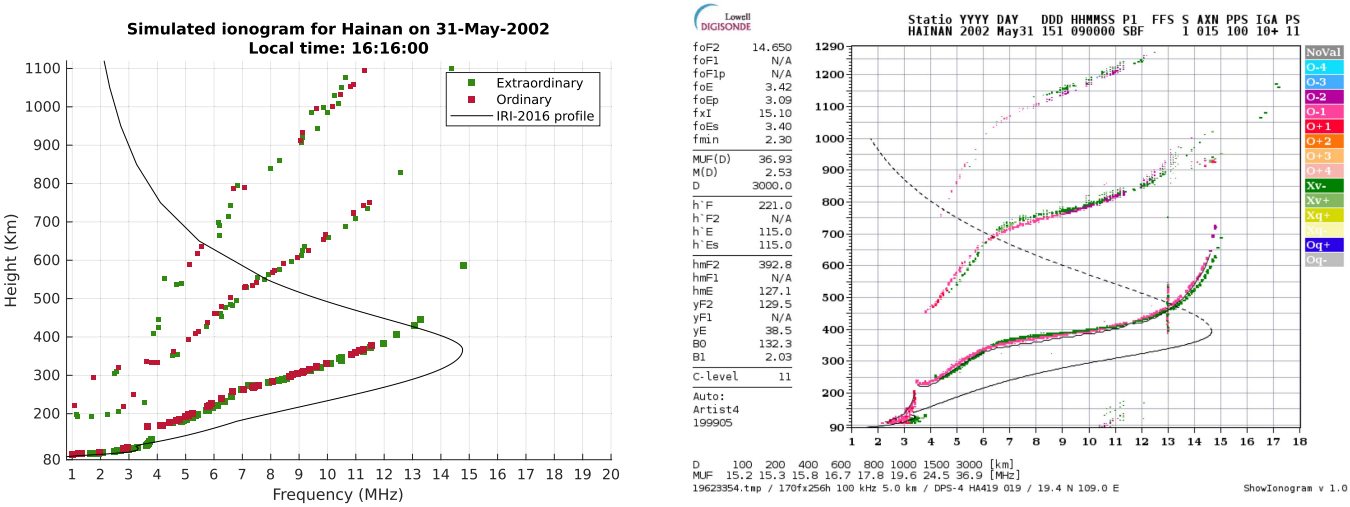

Fig. 18. Simulated ionogram (left) from Hainan, China (19.4° N, 109.0° E) on 31 May 2002 at 9:00 UTC, compared with (right) real data from the ionosonde.

simulations have been conducted by randomly varying the elevation around zenith, and sweeping the frequency from 1 to 16 MHz, depending on the MUF.

To generate the simulated ionograms, for each ray, the virtual height that the ray has reached has been computed as half of the group path, P'. This assumes that the velocity of the wave is always equal to the speed of light in vacuum, which is the common way to compute the altitude in ionograms.

Fig. 18 shows the results of the simulated ionogram (left) for the Hainan island station, Southern China, on 31 May 2002 at 16:16 h LT. Ordinary (in red) and extraordinary (in green) rays are traced, plotting for each of them, a point at its frequency, and its virtual height. The true-altitude plasma density profile is also drawn (black line). On the right plot, the real ionogram from Hainan at the same time is shown.

A clear correspondence between the two plots can be certainly observed. In our simulation, the rays were allowed to bounce up to three times, creating these three strips at different altitudes. They nearly match the ones from the real ionogram, showing their vertical asymptotes at almost the same frequencies, which approaches the critical frequencies of each layer. It is also clear the almost identical shape of the plasma frequency profiles.

Another example of these ionograms is shown in Fig. 19 for the Gakona radio station in Alaska. In this case, being at a much higher latitude, the ionospheric electron density is lower, and so are the plasma frequencies. This means that the MUF is also lower, around 5–6 MHz. In this case, there is a discrepancy between the real data and the simulated ionogram, showing, the last one, lower plasma frequencies, and slightly lower altitude. This is a clear example that the results provided by the simulator may not always fit the ground-truth measurements. This is mainly because the simulator uses standard a climatological ionospheric model, such as IRI, which does not take into account spatiotemporal anomalies coming for example from the space weather, or ionospheric perturbations such as plasma bubbles or depletions.

The results shown in this section are also consistent with the ones obtained by [54], in which they simulate oblique ionograms using a 3-D ray tracer propagator accounting only for the refracting effect of the ionosphere, and the birefringence induced by the magnetic field. They designed and simulated an ionospheric profile with two Gaussian-shape layers, E and F, and a sinusoidal travelling ionospheric disturbances with small-scale irregularities.

TABLE V
COMPARISON OF FORTRAN IONORT OUTPUTS WITH CURRENT SOFTWARE

Ray	f (Hz)	El (°)	Tx (km)	Rx (km)	Delay (ms)	Group path (km)
1	3	10	0	0	3.09	924.97
1	3	10	0	0	3.07	919.05
2	8	-70	550	0	2.80	839.93
2	8	-70	550	0	2.92	876.36
3	20	-30	550	0	5.21	1560.56
3	20	-30	550	0	5.17	1549.88
4	12	30	0	0	4.42	1326.31
4	12	30	0	0	4.40	1317.78

Each second row represents the new software's result.

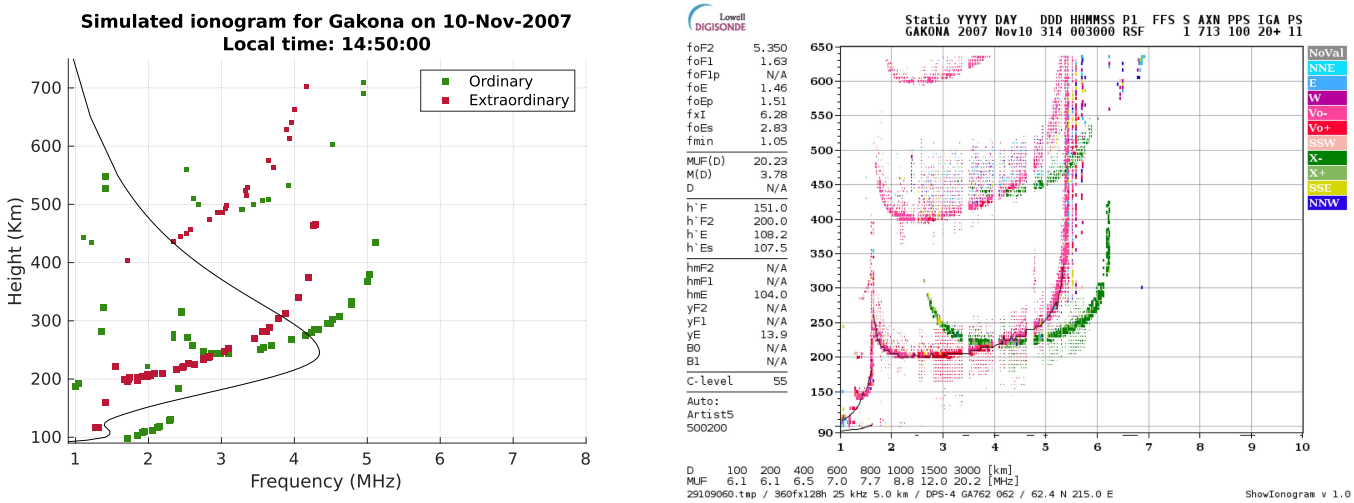

Fig. 19. Simulated ionogram (left) from Gakona, Alaska (62.4° N, 145.0° W) on 10 November 2007 at 00:30 UTC, compared with (right) real data from the ionosonde.

F. Comparison With Older FORTRAN Software

In this section, a comparison between this software simulator and its original version IONORT is shown [17]. The old version has been run using the MATLAB wrapper of the original FORTRAN codes, and the output has been retrieved from the graphical user interface and compared to the output of the same rays traced with the software described in this study. Four case studies have been selected for the date in which the original IONOPROFILE was available, 29 May 2010 12:00:00 UTC. This IONOPROFILE has been retrieved from the text file and injected in the new software, bypassing the IRI-2016 computation.

The results of the simulations of the four rays are shown in Fig. 20. In all cases, the mismatch is minimal. The largest difference is observed for the *ray 2*, which is due to numeric errors induced by the abrupt electron density transition present in the original profile at around 300-km height (see background color in Fig. 20). The rest of configurations are the same: dipole model for the magnetic field and double-exponential electron collision frequency model.

A comparison between the numeric outputs of these simulations are shown in Table V. A variation of around 0.6% is observed between the results of all rays except the *ray2* (4.28%).

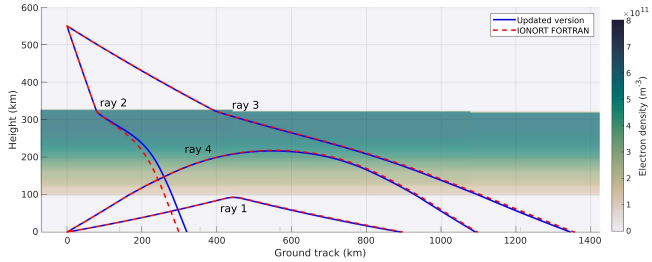

Fig. 20. Comparison of IONORT FORTRAN with current software using the same original ionospheric profile. Red lines represent the older version in FORTRAN, and blue lines are obtained with current software using the default parameters.

IV. CONCLUSION

The development, design, and testing of a ray tracer simulator has been presented in this article. It has been based on an original FORTRAN software that was difficult to maintain and did not include the latest models to describe the ionosphere and the Earth's magnetic field. Several reasons justify the work invested in making this major upgrade, which are as follows.

1) The original software was written in FORTRAN 77 making it difficult to maintain.

2) The original software used static models for the ionospheric density, injected into the program as text files.
3) Modern and updated models of the ionosphere's electron density, Earth's magnetic field, atmospheric density and composition, and ionospheric perturbations were not included.
4) In addition, a model for the EPBs has been included. It implements simple 3-D ellipsoidal bubbles that drift Eastwards and upwards perturbing the rays propagating through them.
5) Accurate measurements of the absorption can be performed using a variety of models enumerated in Table II.
6) Having software able to accurately compute the signal propagation through the ionosphere is very much needed to design upcoming P- and L-bands SAR satellite missions, new radar sounder missions, etc., and to study techniques to mitigate the effects of the ionosphere on them.

The developed software is accurate in a large variety of environments, allowing the simulation of the most common situations for satellite signal propagation, but also, in other environments that are not so usual, allowing the experimentation with new technologies for communications or remote sensing. In particular, it has been proven to work well at frequencies above 2 MHz, even though, as expected, rays do not cross the ionosphere until about 10 MHz, depending on the local electron density profile and incidence angle of the wave. Numerical integration problems are sometimes found in the poles or when the ray is forced to cross the ionosphere with elevations $\sim \pm 90°$, and when the frequency is smaller than the maximum plasma frequency at this location, which would create a highly sharp reflection. Both problems are usually solved by adding a very small increment to either the latitude or the elevation.

Future improvements will include a more refined model for ionospheric bubble's shape and their temporal evolution, and adding an intensity/phase scintillation module such as the one presented in [1] and [55].

The code could also be slightly modified to be used in other planet's ionospheres, helping in the design of interplanetary missions to Mars [56], or giant planets [57], for example. For this, tuning the parameters of magnetic field and electron concentration, and adjusting the dimensions of the system can simulate the behavior of radio signals crossing their ionospheres.

Finally, given that the software is essentially an EM ray tracer propagator through a plasma, this could be used in other scenarios not related to the Earth's ionosphere. In particular, one interesting application is to model the behavior of radio signals through the plasma sheath formed around a spacecraft during its reentry [58], [59].

Appendix
Description of the 3-D EPB Model Implemented

The implemented model is an extension of the 2-D model from [60] by adding the vertical dimension. It estimates the decrement in the electron density in each point of a 3-D grid to be then subtracted from the background profile IONO_PROFILE obtained from the IRI2016 model. The incremental electron density is modeled using

$$\Delta N(x,y,z,t) = \Delta N_{\max} \cdot \exp\left\{-\frac{(t-T_0)^2}{2\,T^2}\right\} \exp\left(-\left[a(x-x_0)^2 - 2b(x-x_0)(y-y_0) + c(y-y_0)^2\right]\right) \exp\frac{-(z-z_0)^2/(2\sigma_z^2)}{\sqrt{2\pi\sigma_z^2}} \cdot f(y) \tag{22}$$

where

$$\sigma_x = \frac{B_d}{6} \tag{23}$$

$$\sigma_y = \frac{B_d \cdot B_{ar}}{6} \tag{24}$$

$$a = \frac{\cos^2(-B_{\text{dec}})}{2\sigma_x^2} + \frac{\sin(-B_{\text{dec}})^2}{2\sigma_y^2} \tag{25}$$

$$b = -\frac{\sin(-2B_{\text{dec}})}{4\sigma_x^2} + \frac{\sin(-2B_{\text{dec}})}{4\sigma_y^2} \tag{26}$$

$$c = \frac{\sin^2(-B_{\text{dec}})}{2\sigma_x^2} + \frac{\cos(-B_{\text{dec}})^2}{2\sigma_y^2} \tag{27}$$

$$f(y) = \begin{cases} 1, & \text{if } |y| \le 30° \\ \cos^2\left(\frac{|y|-30}{5}\frac{\pi}{2}\right), & \text{if } 30° \le |y| \le 35° \\ 0, & \text{if } 35° \le |y|. \end{cases} \tag{28}$$

In these equations, $\Delta N_{\max}$ is the maximum depth of the depletion, T_0 is the time of the maximum depletion, T is the duration of the depletion, (x_0, y_0, z_0) are the initial latitude, longitude, and height of the bubble center, $f(y)$ is an edge-smoothed function limiting the appearance of bubbles to the equatorial region, B_d is the bubble diameter, B_{ar} is the bubble axial-ratio, B_{dec} is the bubble declination, and σ_z is the standard deviation of the vertical Gaussian profile of the bubble, detailed latter.

In this expression, $\Delta N_{\max}$ can be computed if all the bubble parameters are known. However, the bubble's information extracted from Blanch et al. [32] only provides 2-D dimensions of the bubble, i.e., neither the vertical center of the bubble (z_0) nor its vertical extension (σ_z). Consequently, to completely implement the bubble perturbations into the ionospheric propagator, a 3-D model has been created. For the sake of simplicity, a simple ellipsoidal shape model has been implemented, as adding complexity in the vertical component does not make sense without increasing the complexity in the horizontal component too.

The main problem encountered during its creation was the adequate estimation of the vertical size and position of the bubble. Even in the case of having a $\Delta N_{\max}$ larger than the local TEC at the bubble coordinates, if the bubble parameters mentioned before (vertical size and height of the center) are not carefully selected, negative values in the resulting electron density profile can appear. This behavior is described in Fig. 21, where several iterations help to get to a solution for this issue.

In the algorithm designed, the height of the center of the bubble (z_0) has been located at the intermediate point of the full-width at half maximum (FWHM) interval, while the Gaussian

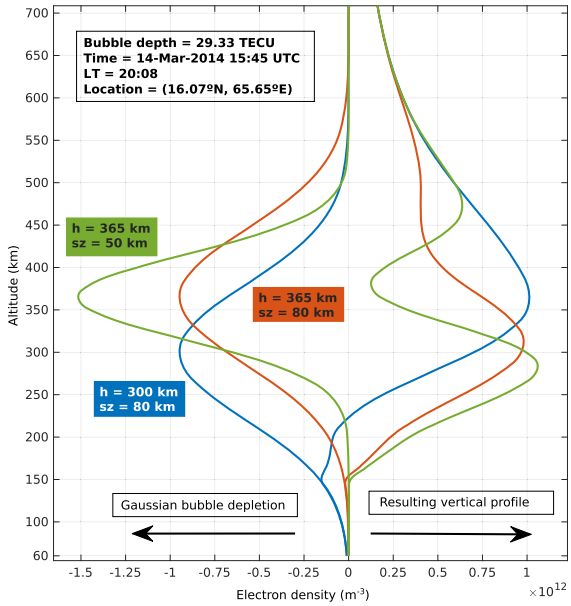

Fig. 21. Results of the ionospheric profile after using different bubble's vertical size parameters. Blue: The center of the bubble is too low (negative values from 0 to 200 km). Red: Adequate height of the bubble, but too wide (negative values around 150 km). Green: Adequate bubble's size and position.

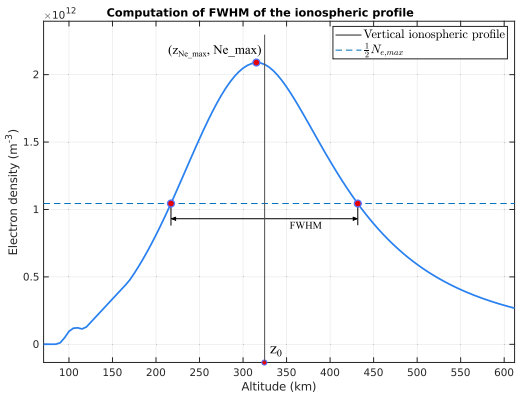

Fig. 22. Diagram to compute the standard deviation and center of the bubbles.

standard deviation of the bubble (σ_z) is proportional to standard deviation of the equivalent Gaussian ionospheric profile having the same FWHM.

$$\sigma_z = m\,\sigma_{z,\text{iono}} \tag{29}$$

$$\sigma_{z,\text{iono}} = \frac{\text{FWHM}}{2\sqrt{2\log 2}}. \tag{30}$$

Fig. 22 explains the way to compute the standard deviation of the Gaussian profile of the bubbles derived from the local ionospheric profile, computed with IRI at the bubble location. Fig. 23 shows the results for different values of the m parameter. It has been observed that a value of $m = 0.6$ is reasonable to correctly model the bubbles. Note that if m is too small, the peak density of the bubble at z_0 increases and may produce negative values in the resulting electron density. On the other hand, larger values of m will produce wider bubbles that can also create negative values, in this case, at the edges of the profile, usually around 100–150 km.

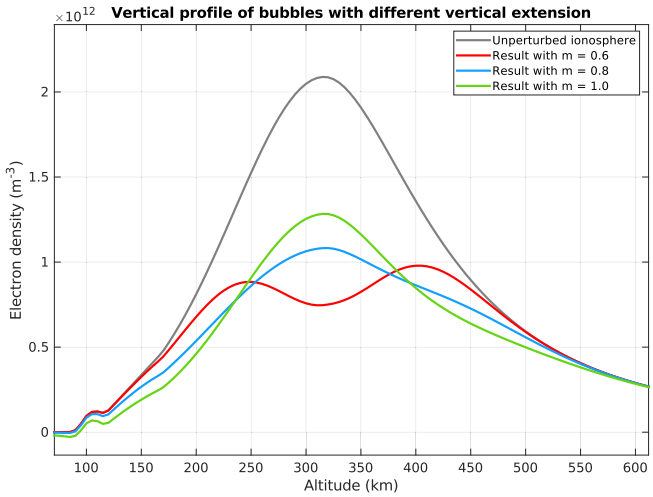

Fig. 23. Results for different values of the proportionality parameter m.

In addition, the traveling velocities of the bubbles have been modeled too. The horizontal velocity is derived from the statistical results of [32], traveling eastwards following the lines of a constant geomagnetic field with a value of (97.4 ± 35.8) m/s. The vertical drift was derived according to the model from [61], in which the bubble rise velocity is given by the ratio between the local gravity (g) and the electron collision frequency (ν_{eff}) as follows:

$$v_{\text{vert}} = \frac{g}{\nu_{\text{eff}}}. \tag{31}$$

REFERENCES

[1] A. Camps, J. Barbosa, I. Nestoras, A. Jordao, M. Sanjuan-Ferrer, and M. Rodriguez-Cassola, "Biomass end-to-end performance simulator: Description of the ionosphere module," in *Proc. IEEE Int. Geosci. Remote Sens. Symp.*, 2021, pp. 2266–2269.

[2] P. Hernández, C. Molina, and A. Camps, "Simulación física del centelleo ionosférico para constelaciones LEO-PNT," in *Proc. 39th Simposio Nacional de la Unión Científica Internacional de Radio*, Cuenca, Spain, 2024.

[3] C. Molina and A. Camps, "Ionospheric effects on VHF radar sounder missions," presented at the IEEE Int. Geosci. Remote Sens. Symp., Jul. 2024.

[4] Y. Osawa, "Optical and microwave sensor on Japanese mapping satellite—ALOS," *Int. Arch. Photogramm. Remote Sens. Spat. Inf. Sci*, vol. 35, pp. 309–312, 2004.

[5] M. Davidson, N. Gebert, and L. Giulicchi, "ROSE-L—The L-band SAR Mission for Copernicus," in *Proc. 13th Eur. Conf. Synthetic Aperture Radar*, 2021, pp. 1–2.

[6] P. A. Rosen, Y. Kim, R. Kumar, T. Misra, R. Bhan, and V. R. Sagi, "Global persistent SAR sampling with the NASA-ISRO SAR (NISAR) mission," in *Proc. IEEE Radar Conf.*, 2017, pp. 0410–0414.

[7] A. E. Giraldez, "SAOCOM-1 Argentina L-Band SAR mission overview," in *Proc. 2nd Workshop Coastal Mar. Appl. SAR*, H. Lacoste, Ed., Svalbard, Norway, vol. 565, Jun. 2004, Paper 27. [Online]. Available: https://ui.adsabs.harvard.edu/abs/2004ESASP.565E..27G/abstract

[8] T. Le Toan et al., "The BIOMASS mission: Mapping global forest biomass to better understand the terrestrial carbon cycle," *Remote Sens. Environ.*, vol. 115, no. 11, pp. 2850–2860, 2011.

[9] S. Quegan et al., "The European space agency BIOMASS mission: Measuring forest above-ground biomass from space," *Remote Sens. Environ.*, vol. 227, pp. 44–60, 2019.

[10] R. Jordan et al., "The Mars express MARSIS sounder instrument," *Planet. Space Sci.*, vol. 57, no. 14–15, pp. 1975–1986, 2009.

[11] R. Seu et al., "SHARAD: The MRO 2005 shallow radar," *Planet. Space Sci.*, vol. 52, no. 1–3, pp. 157–166, 2004.

[12] A. Freeman, X. Pi, and E. Heggy, "Radar sounding through the Earth's ionosphere at 45MHz," *IEEE Trans. Geosci. Remote Sens.*, vol. 55, no. 10, pp. 5833–5842, Oct. 2017.

[13] C. L. Rino, "A power law phase screen model for ionospheric scintillation: 1. weak scatter," *Radio Sci.*, vol. 14, no. 6, pp. 1135–1145, 1979.

[14] R. M. B. James and A. Secan, *An Improved Model of High-Latitude F-Region Scintillation (WBMOD Version 13)*. Seattle, WA, USA: Northwest Research Associates, 1994.

[15] *Ionosphere Modular Software Package (IMSP MGS)*, Apr. 29, 2024. [Online]. Available: https://essr.esa.int/project/ionosphere-modular-software-package-imsp-mgs

[16] R. M. Jones and J. J. Stephenson, "A versatile three-dimensional ray tracing computer program for radio waves in the ionosphere," Office of Telecommunications, U. S. Dept. of Commerce, Washington, DC, USA, Oct. 1975.

[17] A. Azzarone, C. Bianchi, M. Pezzopane, M. Pietrella, C. Scotto, and A. Settimi, "IONORT: A windows software tool to calculate the HF ray tracing in the Ionosphere," *Comput. Geosci.*, vol. 42, pp. 57–63, 2012.

[18] A. Settimi et al., "Testing the IONORT-ISP system: A comparison between synthesized and measured oblique ionograms," *Radio Sci.*, vol. 48, no. 2, pp. 167–179, 2013.

[19] A. Settimi, M. Pietrella, M. Pezzopane, and C. Bianchi, "The IONORT-ISP-WC system: Inclusion of an electron collision frequency model for the D-layer," *Adv. Space Res.*, vol. 55, no. 8, pp. 2114–2123, 2015.

[20] E. Erdem, F. Ankan, M. N. Deviren, and I. Çor, "A model based ray tracing algorithm for anisotropic and inhomogeneous ionosphere with GIM-TEC assimilation," in *Proc. 7th Int. Conf. Recent Adv. Space Technol.*, 2015, pp. 477–481.

[21] E. Erdem and F. Arikan, "IONOLAB-RAY: A wave propagation algorithm for anisotropic and inhomogeneous Ionosphere," *Turkish J. Elect. Eng. Comput. Sci.*, vol. 25, pp. 1712–1723, 2017.

[22] U. Sezen, O. Sahin, F. Arikan, and O. Arikan, "Estimation of $hmf2$ and $fof2$ communication parameters of ionosphere $f2$-layer using GPS data and IRI-Plas model," *IEEE Trans. Antennas Propag.*, vol. 61, no. 10, pp. 5264–5273, Oct. 2013.

[23] P. Alken et al., "International geomagnetic reference field: The thirteenth generation," *Earth, Planets Space*, vol. 73, no. 1, pp. 1–25, Feb. 2021.

[24] J. Picone, A. Hedin, D. P. Drob, and A. Aikin, "NRLMSISE-00 empirical model of the atmosphere: Statistical comparisons and scientific issues," *J. Geophys. Res., Space Phys.*, vol. 107, no. A12, pp. SIA–15, 2002.

[25] D. Bilitza et al., "International reference ionosphere 2016: From ionospheric climate to real-time weather predictions," *Space Weather*, vol. 15, no. 2, pp. 418–429, 2017.

[26] B. Nava, P. Coisson, and S. Radicella, "A new version of the NeQuick ionosphere electron density model," *J. Atmospheric Solar-Terrestrial Phys.*, vol. 70, no. 15, pp. 1856–1862, 2008.

[27] K. G. Budden, *The Propagation of Radio Waves: The Theory of Radio Waves of Low Power in the Ionosphere and Magnetosphere*. Cambridge, U.K.: Cambridge Univ. Press, 1988.

[28] H. Sen and A. Wyller, "On the generalization of the Appleton-Hartree magnetoionic formulas," *J. Geophys. Res.*, vol. 65, no. 12, pp. 3931–3950, 1960.

[29] E. W. Weisstein, "Runge-Kutta method," in *MathWorld–A Wolfram Web Resource*, 2013. Accessed: Jul. 30, 2009. [Online]. Available: http://mathworld.wolfram.com/Runge-KuttaMethod.html

[30] F. Bashforth and J. C. Adams, *An Attempt to Test the Theories of Capillary Action by Comparing the Theoretical and Measured Forms of Drops of Fluid*. Cambridge, U.K.: University Press, 1883.

[31] F. R. Moulton, *New Methods in Exterior Ballistics*. St. Chicago, IL, USA: Univ. Chicago Press, 1926.

[32] E. Blanch et al., "Improved characterization and modeling of equatorial plasma depletions," *J. Space Weather Space Climate*, vol. 8, 2018, Art. no. A38.

[33] IRI2016 ionosphere model from Python and Matlab (space-physics/iri2016), Feb. 27, 2018. [Online]. Available: https://github.com/space-physics/iri2016

[34] M. Moussa, CCMC. IRI-2016 Web Model. Accessed: Jul. 18, 2024. [Online]. Available: https://ccmc.gsfc.nasa.gov/modelweb/models/iri2016_vitmo.php

[35] M. C. Kelley, J. J. Makela, L. J. Paxton, F. Kamalabadi, J. M. Comberiate, and H. Kil, "The first coordinated ground- and space-based optical observations of equatorial plasma bubbles," *Geophys. Res. Lett.*, vol. 30, no. 14, 2003, Art. no. 1766.

[36] H. Kil, R. A. Heelis, L. J. Paxton, and S.-J. Oh, "Formation of a plasma depletion shell in the equatorial ionosphere," *J. Geophys. Res. Space Phys.*, vol. 114, no. A11, 2009, Art. no. A11302.

[37] H. Kil, "The morphology of equatorial plasma bubbles—A review," *J. Astron. Space Sci.*, vol. 32, no. 1, pp. 13–19, Mar. 2015.

[38] T. Yokoyama, H. Shinagawa, and H. Jin, "Nonlinear growth, bifurcation, and pinching of equatorial plasma bubble simulated by three-dimensional high-resolution bubble model," *J. Geophys. Res. Space Phys.*, vol. 119, no. 12, pp. 10–474, 2014.

[39] T. Yokoyama, "A review on the numerical simulation of equatorial plasma bubbles toward scintillation evaluation and forecasting," *Prog. Earth Planet. Sci.*, vol. 4, pp. 1–13, 2017.

[40] T. Yokoyama, H. Jin, H. Shinagawa, and H. Liu, "Seeding of equatorial plasma bubbles by vertical neutral wind," *Geophys. Res. Lett.*, vol. 46, no. 13, pp. 7088–7095, 2019.

[41] T. Yokoyama, "Simulation data used for publication 'Seeding of equatorial plasma bubbles by vertical neutral wind' by Yokoyama et al.," Zenodo, May 13, 2019, doi: 10.5281/zenodo.2782922.

[42] A. Zmuda, "The international geomagnetic reference field 1965.0: Introduction," *Bull. Int. Assoc. Geomag. Aeron.*, vol. 28, pp. 148–152, 1971.

[43] E. Thébault et al., "International geomagnetic reference field: The 12th generation," *Earth, Planets Space*, vol. 67, no. 1, pp. 1–19, 2015.

[44] A. Chulliat, P. Alken, and M. Nair, "The US/UK world magnetic model for 2020-2025," Tech. Rep., 2020. [Online]. Available: https://doi.org/10.25923/ytk1-yx35

[45] NCEI Geomagnetic Modeling Team, British Geological Survey, "2019: World Magnetic Model 2020," NOAA National Centers for Environmental Information, 2019. Accessed: Jul. 18, 2024. [Online]. Available: https://doi.org/10.25921/11v3-da71

[46] J.-F. Oehler, D. Rouxel, and M.-F. Lequentrec-Lalancette, "Comparison of global geomagnetic field models and evaluation using marine datasets in the north-eastern atlantic ocean and western M sea," *Earth, Planets Space*, vol. 70, no. 1, pp. 1–15, 2018.

[47] M. Nicolet, "The collision frequency of electrons in the ionosphere," *J. Atmospheric Terr. Phys.*, vol. 3, no. 4, pp. 200–211, May 1953.

[48] J. B. Fisk, "Theory of the scattering of slow electrons by diatomic molecules," *Phys. Rev.*, vol. 49, no. 2, pp. 167–173, Jan. 1936, doi: 10.1103/PhysRev.49.167.

[49] R. Schunk and A. Nagy, *Ionospheres: Physics, Plasma Physics, and Chemistry, Cambridge Atmospheric and Space Science Series*. Cambridge, U.K.: Cambridge Univ. Press, 2009.

[50] P. Banks, "Electron thermal conductivity in the ionosphere," *Earth Planet. Sci. Lett.*, vol. 1, no. 4, pp. 151–154, Jul. 1966.

[51] M. Mahooti, "NRLMSISE-00 atmosphere model," MATLAB Central File Exchange, 2022. [Online]. Available: https://www.mathworks.com/matlabcentral/fileexchange/56253-nrlmsise-00-atmosphere-model

[52] B. W. Reinisch and I. A. Galkin, "Global ionospheric radio observatory (GIRO)," *Earth, Planets, Space*, vol. 63, pp. 377–381, 2011.

[53] I. A. Galkin and B. W. Reinisch, "Global ionospheric radio observatory (GIRO): Status and prospective," in *Proc. 30th URSI Gen. Assem. Sci. Symp.*, 2011, pp. 1–4.

[54] H. Song, H. Qing, and X. Zou, "A parallel optimization 3D numerical ray-tracing method for the fast and accurate simulation of disturbed oblique ionogram," *Adv. Space Res.*, vol. 70, no. 10, pp. 2894–2904, 2022.

[55] A. Camps et al., "Updated ionospheric module for ESA biomass mission end-to-end performance simulator," in *Proc. IEEE Int. Geosci. Remote Sens. Symp.*, 2023, pp. 7673–7676.

[56] B. Sánchez-Cano, "Mars' ionosphere: The key for systematic exploration of the red planet," *Front. Astron. Space Sci.*, vol. 9, 2023, Art. no. 1101945.

[57] S. Miller, A. Aylward, and G. Millward, "Giant planet ionospheres and thermospheres: The importance of ion-neutral coupling," *Space Sci. Rev.*, vol. 116, pp. 319–343, 2005.

[58] H. Zhou, X. Li, K. Xie, Y. Liu, and Y. Yu, "Mitigating reentry radio blackout by using a traveling magnetic field," *AIP Adv.*, vol. 7, no. 10, 2017, Art. no. 105314.

[59] R. Hartunian et al., "Implications and mitigation of radio frequency blackout during reentry of reusable launch vehicles," in *Proc. AIAA Atmospheric Flight Mechanics Conf. Exhibit.*, doi: 10.2514/6.2007-6633.

[60] A. Camps et al., "Improved modelling of ionospheric disturbances for remote sensing and navigation," in *Proc. IEEE Int. Geosci. Remote Sens. Symp.*, 2017, pp. 2682–2685.

[61] D. Anderson and G. Haerendel, "The motion of depleted plasma regions in the equatorial ionosphere," *J. Geophys. Res., Space Phys.*, vol. 84, no. A8, pp. 4251–4256, 1979.

Carlos Molina was born in Seville, Spain, in 1990. He received the degree in physics from the Universidad de Sevilla, Seville, in 2018, the master's degree in space and aeronautical engineering in 2019 from the Universitat Politécnica de Catalunya (UPC), Barcelona, Spain, where since 2019 he has been working toward the Ph.D. degree in signal theory and communications, under the guidance of A. Camps and H. Park.

From 2014 to 2018, he worked as a Microelectronics Engineer and Layout Technician with Teledyne Anafocus, a microelectronics company working on the design and manufacturing of custom smart CMOS image sensors. His master's thesis was with NanoSat Lab, UPC, which involved designing and manufacturing an onboard computer module for CubeSats and included schematics and layout design, as well as printed circuit board integration. During his Ph.D., he worked on several projects, including developing an ionospheric ray tracer simulator as part of an ESA project. His research focuses on investigating ionospheric perturbations and their impact on radio wave propagation using GNSS remote sensing techniques. He is particularly interested in the interaction between the ionosphere and the lithosphere. He also used a neural network approach to emulate the results of the WBMOD ionospheric scintillation model. In addition, he participated in the development of the RITA mission from the NanoSat Lab, where he was the in charge of a multispectral CMOS camera and optics for a 3U Cubesat.

Elena Fernández-Niño was born in Barcelona, Spain. She received the B.S. degree in telecommunications engineering specialized in the field of telecommunications systems and the M.S. degree in telecommunications engineering specialized in antennas, microwaves, and photonics for communications and Earth observation, both from the Universitat Politécnica de Catalunya (UPC), Barcelona, in 2019 and 2022, respectively. She is currently working toward the Ph.D. degree in space communications with the i2CAT Foundation, Barcelona.

She joined the NanoSat Lab-UPC in 2019 as a System Engineer to develop her B.S. thesis, where she conducted a feasibility analysis of an Earth observation mission using passive microwave radiometry from a CubeSat, NanoSat Lab-UPC, Barcelona. In 2022, she developed her M.S. thesis participating in an ESA project as a Software Developer to implement an ionospheric ray tracer simulator, NanoSat Lab-UPC. She is currently designing and implementing a hybrid intersatellite communications system with i2CAT Foundation. Her research interests include design and analysis of a satellite mission, intersatellite communications, optical space communications, satellite networks, and ionospheric effects over RF signals.

Adriano Camps received the Ph.D. degree in telecommunications engineering from the Universitat Politécnica de Catalunya (UPC), Barcelona, Spain, in 1996.

His Ph.D. thesis was about the MIRAS instrument, which became the single payload of European Space Agency's (ESA) Soil Moisture and Ocean Salinity (SMOS) mission. He joined the Electromagnetics and Photonics Engineering Group, Department of Signal Theory and Communications, UPC, as an Assistant Professor in 1993, an Associate Professor in 1997, and a Full Professor in 2007. In 1999, he was on sabbatical leave with the Microwave Remote Sensing Laboratory, University of Massachusetts, Amherst, MA, USA. He has authored and coauthored more than 250 papers in peer-reviewed journals, nine book chapters, and the book titled *Introduction to Satellite Remote Sensing: Atmosphere, Ocean, Land and Cryosphere Applications* (Elsevier, 2017), and more than 500 conference presentations. According to Google Scholar/Scopus, his H-index is 62/48, and his publications have received more than 15 135/10 447 citations. He holds 12 patents and has advised 28 Ph.D. thesis students (more than eight ongoing), and more than 150 final projects and M.Eng. theses. He was the Scientific Coordinator of the CommSensLab Research Center (María de Maeztu Excellence Research unit), Department of Signal Theory and Communications, in 2016–2020. Within CommSensLab, he coleads the Remote Sensing Lab, and leads the UPC NanoSat Lab. His research interests include microwave remote sensing, with special emphasis in microwave radiometry by aperture synthesis, remote sensing using signals of opportunity (GNSS-R), radio frequency interference detection and mitigation, and nanosatellites as a tool to test innovative remote sensors.

Dr. Camps is the Principal Investigator of the first four UPC nanosatellites, including FSSCat the first mission contributing to the Copernicus System based on CubeSats and it has produced for the first time using CubeSats scientific quality soil moisture, sea ice extent, concentration and thickness, and sea salinity maps in the Arctic. He was the Chair of the uCal 2001, a Technical Program Committee Co-Chair of International Geoscience and Remote Sensing Symposium (IGARSS) 2007, a Co-Chair of GNSS-R 2010, a General Co-Chair of the IGARSS 2020 of the 6th Fractionated and Federated Satellite Systems Workshop, and a Member of the Local Organising Committee (LOC) of ESA 4th Symposium on Space Educational Activities (SSEA) held in Barcelona in 2022.